Bing Yao

Department of Industrial and Manufacturing Engineering, The Pennsylvania State University, University Park, PA 16802

Farhad Imani

Department of Industrial and Manufacturing Engineering, The Pennsylvania State University, University Park, PA 16802

Aniket S. Sakpal

Department of Industrial and Manufacturing Engineering, The Pennsylvania State University, University Park, PA 16802

E. W. Reutzel

Applied Research Laboratory The Pennsylvania State University, P.O. Box 30, State College, PA 16804-0030

Hui Yang¹

Department of Industrial and Manufacturing Engineering, The Pennsylvania State University, University Park, PA 16802 e-mail: huy25@psu.edu

Multifractal Analysis of Image Profiles for the Characterization and Detection of Defects in Additive Manufacturing

Metal-based powder-bed-fusion additive manufacturing (PBF-AM) is gaining increasing attention in modern industries, and is a promising direct manufacturing technology. Additive manufacturing (AM) does not require the tooling cost of conventional subtractive manufacturing processes, and is flexible to produce parts with complex geometries. Quality and repeatability of AM parts remain a challenging issue that persistently hampers wide applications of AM technology. Rapid advancements in sensing technology, especially imaging sensing systems, provide an opportunity to overcome such challenges. However, little has been done to fully utilize the image profiles acquired in the AM process and study the fractal patterns for the purpose of process monitoring, quality assessment, and control. This paper presents a new multifractal methodology for the characterization and detection of defects in PBF-AM parts. Both simulation and real-world case studies show that the proposed approach effectively detects and characterizes various defect patterns in AM images and has strong potential for quality control of AM processes. [DOI: 10.1115/1.4037891]

1 Introduction

Additive manufacturing (AM), also known as three-dimensional (3D) printing, is a process to produce a 3D part with complex geometries layer by layer from the computer-aided design (CAD) models. Metal-based powder-bed-fusion additive manufacturing (PBF-AM) provides an opportunity for modern industries to produce arbitrarily complex, engineered geometries, such as intricate internal features, lattice structures, and honeycomb structures, directly from a 3D CAD model [1]. Moreover, it also shows many other capabilities such as reduced material waste, part consolidation, and exemption of expensive part-specific tooling cost, which cannot be achieved otherwise with traditional manufacturing techniques.

However, many technical challenges still hamper the widespread adoption of AM. Quality and repeatability remain to be challenging in the implementation of AM technology, which has not yet been fully addressed to meet the industrial requirements. Processing parameters such as laser power, scan velocity, and hatch spacing will impact the quality of final builds. Note that AM decomposes the 3D CAD model into a series of two-dimensional (2D) cross layers, and then materials are added layer by layer to build the physical part. Defects often occur in the build component due to the discontinuity of the printing process and other extraneous factors in the process. There are different types of defects/discontinuities encountered in AM. For example, Tammas-Williams et al. [2] showed that pore defects generally originate from trapped gas in the selective-electron-beam-melting process due to partially unmelted powders under an inefficient melting regime with a low-power laser. The "balling" defect is due to a laser with high power environment, where the powder

material fused together excessively driven by surface tension to form spheres that exceed the layer thickness. Li et al. [3] showed that similar phenomenon of balling happened in stainless steel powders in a lower power environment. Crack is the third type of typical defects in AM processes, which occurs due to the variation of gradient of internal thermal stress produced through the process [4]. As the material is heating and cooling layer by layer, the gradient of thermal stresses varies rapidly, leading to the AM part cracking near the substrate interface or other areas of high residual

Rapid advancements in sensing technology provide an opportunity to realize high levels of quality control of AM parts. There is an urgent need to extract useful information from rich sensing data and then correlate them with quality characteristics of AM build, e.g., geometric accuracy, surface finish, and mechanical properties. This is conducive to improve the quality and repeatability of AM products. Rao et al. [5] analyzed the heterogeneous sensor data captured by thermocouples, accelerometers, and infrared temperature sensor to identify failure modes and detect the onset of process anomalies in AM processes. Chivel and Smurov [6] integrated industrial selective-laser-sintering/melting machines with optical systems to acquire images of the distribution and maximum value of surface temperature of each layer to control thermal effects in AM processes. The center for innovative material processing through direct digital deposition (CIMP-3D) at the Pennsylvania State University developed an optical layer-wise imaging technique to monitor the power-bed-fusion AM process using a consumer-grade 36.3 megapixel digital single-lens reflex camera [7]. Among these various sensing modalities and systems, image sensing gains special attention for process monitoring and control of AM processes due to rich process information and low implementation cost. However, realizing the full potentials of rich imaging data depends to a great extent on the information processing for AM quality control. Few, if any, previous works have

¹Corresponding author.

Manuscript received July 18, 2017; final manuscript received August 30, 2017; published online January 3, 2018. Assoc. Editor: Zhijian J. Pei.

considered the characterization of fractal patterns in image profiles for the monitoring and control of AM processes.

This paper presents a novel multifractal methodology to characterize and model image profiles for quality control in AM processes. First, we introduce the fractal dimension to characterize and quantify irregular patterns and behaviors of AM image profiles. Second, we show that a single exponent (fractal dimension) is limited and further extract the new multifractal spectrum to describe complex fractal behaviors of image profiles in AM processes. Third, we extract the Hotelling T^2 statistics from multifractal features for defect characterization and detection in AM image profiles, and further correlate the Hotelling T^2 statistics with process parameters (i.e., hatch spacing, scan velocity, and laser power) using multivariate regression analysis. Case studies on both simulation and real-world AM processes show that the proposed approach effectively characterizes and detects various defect patterns in AM images and has strong potential for quality control in real PBF-AM applications.

This paper is organized as follows: Sec. 2 presents the state of the art in imaging sensing and image-based quality control in additive manufacturing. Section 3 introduces the multifractal methodology. Section 4 and 5 present the experimental design and results, and Sec. 6 concludes this presented research.

2 Research Background

2.1 Image Sensing of Additive Manufacturing. Additive manufacturing techniques, often referred as rapid prototyping and rapid manufacturing, offer the capability of manufacturing 3D devices and products with complex geometry directly from CAD models, without extensive machining. Image sensing of AM processes plays an important role in the quality control of small and highly complex AM parts.

The quality of final AM parts is highly dependent on the precise control of process variables such as laser power, scan velocity, and hatch spacing. Sensing systems have been widely used to monitor and control machine variables in AM processes. Kleszczynski et al. [8] used a high-resolution charge-coupled device camera to detect errors in process stability (e.g., insufficient powder, poor supports, or coater damage) and improve part quality. Bi et al. [9] used a photodiode to monitor the reflected laser light from the protective glass and detect possible damages in the protective cover lens that often causes distorting and attenuation of the laser beam. Reutzel and Nassar [10] built an imaging system with a filtered camera to inspect powder delivery and flow characteristics for the detection of damaged or clogged nozzles that introduces inconsistencies in the quality of AM products.

In addition, various thermal and optical devices are used to monitor in-process temperature distribution and layer-by-layer finishes for quality control of final AM builds. The infrared camera is used to capture temperature distribution of 3D printed parts, which contains invaluable information related to residual stress and microstructures of fabricated products, and can be further implemented to monitor and control AM processes. Krauss et al. [11] monitored the temperature distribution of 3D printing layers in the selective laser melting process using an infrared camera, and detected material discontinuities and process deviations caused by random process errors or drifts in process parameters. Rodriguez et al. [12] acquired the absolute temperature of melted or solid surfaces layer by layer in PBF-AM processes using in situ thermography, and further used the infrared images to identify absolute thermal nonuniformity of the part's layer surface for the quality control of AM processes.

High-speed and high-resolution cameras with visible wavelength have also been implemented for directly imaging defects in AM layers to detect process errors and material discontinuities. Jacobsmühlen et al. [13] built a high-resolution imaging device to inspect laser-beam-melting systems. Their imaging system was formed by a monochrome 29 megapixel charge-coupled device

camera, and was able to identify topological flows and control the quality of 3D layers. Foster et al. [7] collected in-process images of layer-by-layer finishes of AM parts both after laser exposure and after recoating using a high-definition 36.3 megapixel digital single-lens reflex camera (Nikon D800E) with multiple flash modules. Grasso et al. [14] monitored the selective-laser-melting process using a high-speed camera, i.e., an Olympus I-speed 3 camera, and showed that this imaging system was able to provide AM images to detect and localize defects caused by overheating phenomena.

Industrial computed tomography (CT) scanning is also widely implemented to inspect the quality of final AM builds. The X-rays in a CT scanner are directed at the parts to capture images related to the internal and external structures of AM builds. There are several hundreds to thousands of 2D X-ray images to reconstruct the 3D structure of AM parts. For example, Pavan et al. [15] proposed an X-ray CT-based quality control approach to analyze porosity and shape deviation in polymers AM process using laser sintering. Dewulf et al. [16] proposed to use X-ray CT-scan to investigate the impact of laser-sintering scanning parameters on the distribution of pores in the polyamide-12 parts.

Layer-wise image profiles produced in 3D printing processes contain rich information related to structures of AM products. It is imperative to extract useful information from image profiles to identify internal defects, i.e., balling, pores, and cracks, in AM parts, which is critical for the optimal design of AM processes and effective control of process parameters such as laser power, scan velocity, and hatch spacing.

2.2 Image-Based Quality Control. The methods of image-based quality control involve a sequence of steps, i.e., image acquisition, image preprocessing, feature extraction, and process monitoring and control. First, image profiles are preprocessed before extracting useful information, e.g., background separation, de-noising, and image compression. Next, quality-related features and characteristics are extracted to represent input images. Finally, the extracted features are further reduced into a smaller set of quality statistics (or variables) for process monitoring and control. A thorough review on different methods of image-based quality control can be referred to Ref. [17]. Some commonly used image-based methods are introduced as follows.

Univariate control charts are usually designed for monitoring image profiles. For example, Nembhard and Kao [18] developed a forecasting algorithm to monitor color transitions in plastic extrusion processes. The exponentially weighted moving average control charts were integrated with the forecasting system to identify the end of the color transition stage. Liang and Chiou [19] used X-bar control charts with 3σ limits to automatically monitor the tool wear of coated drills. However, univariate control charts only monitor one characteristic at a time, which disregards significant information contained in the images. In order to address the limitations in univariate control charts, multivariate control charts are used to monitor more than one quality characteristic simultaneously. Graham et al. [20] used principal component analysis to measure the ladle eye phenomenon in metallurgy, and then applied Hotelling T^2 control charts to monitor the validity of their ladle eye area predictions. Although multivariate charts consider multiple characteristics of the image data, they do not specifically consider the spatial information of image profiles.

Furthermore, spatial control charts have also been proposed to detect the location of defects in the images. For example, Jiang et al. [21] combined analysis of variance with spatial control charts, i.e., exponentially weighted moving average charts, to inspect the uniformity of high-grade liquid crystal display monitors and detect the type, size, and location of defects. Kam et al. [22] proposed to assess the spatial uniformity of particle distributions based on scanning electron microscope images to conduct quality control in manufacturing processes. The images were first preprocessed into binary images with black particles representing the original morphology. Then, the spatial uniformity of these

031014-2 / Vol. 140, MARCH 2018

images was assessed according to the global Shannon entropy measure. Yan et al. [23] developed an image-based process monitoring approach by assessing the spatial and color information of image data using low-rank tensor decomposition. Kan and Yang [24,25] proposed a dynamic network scheme to represent, model, and control time-varying image profiles. A new network-generalized likelihood ratio chart was developed to detect the change point in the underlying dynamics of complex processes. However, these methods do not account for nonlinear and fractal patterns in real-world images. Very little has been done to characterize multifractal patterns in image profiles for quality monitoring and control of AM processes.

2.3 Fractal Patterns of AM Images. It is well known that the natural world surrounding us typically consists of complex, rough, and ragged surfaces, which are often referred as fractal surfaces. Various physical objects demonstrate fractal behaviors. For example, mountain terrains and natural soil structures generally exhibit self-similarity across spatial scales. The human heart is formed of a fractal network of myocardium cells. Fine surface textures in manufacturing demonstrate fractal behaviors over a range of scales [26]. Posadas et al. [27] investigated the fractal patterns in soil images to quantify the soil properties and characterize different soil pore systems. Yang and Chen proposed the fractal approach to analyzing irregular patterns in physiological signals for real-time monitoring of patient conditions [28] and further develop simulation models of reaction–diffusion dynamics on fractal surfaces, which is implemented to model the propagation and conduction of electrical waves in the human heart [29]. In addition, Kan et al. and Chen et al. investigated the fractal patterns in the vibration signals to predict the quality of surface finishes in ultraprecision machining processes [30,31].

Although many of the AM parts appear to have smooth surfaces with visual inspection, nonlinearity and irregularity are inherent to the structure of AM parts. Imaging sensing systems capture process dynamics of every layer in AM builds in the form of 2D image profiles. Each layer of AM processes is rough and, under oblique lighting conditions, appears irregular under high-resolution cameras. In order to demonstrate the roughness and nonlinear patterns of layer surfaces in AM processes, we have simulated three different types of surfaces, i.e., rough, sinusoidal, and random variations, as shown in Figs. 1(a)-1(c), where the value of z-coordinate represents the surface roughness. Note that the pixel intensity of 2D images in Figs. 1(d)-1(f) is proportional to the surface roughness. Later, we will show that fractal analysis

effectively quantifies the nonlinear patterns in these image profiles and is able to differentiate different types of anomalies.

It may be noted that a single fractal dimension was used to investigate the scale effects in surface metrology, and experimental results showed that scale-invariant parameters may not be the best means for surface characterization in the traditional manufacture [26,32]. However, very little has been done to study the multifractal spectrum in manufacturing metrology. Notably, multifractal analysis focuses on the nonlinear patterns (i.e., irregularity, singularity) in the image profiles, rather than a single fractal dimension for scale-invariant characterization of engineered surfaces. In addition, there are few, if any, other investigations of image-based process monitoring in additive manufacturing that monitor and assess fractal patterns or multifractal behaviors of AM image profiles. Therefore, we propose to investigate the multifractal spectrum of image profiles for the process monitoring and quality control in PBF-AM processes.

3 Multifractal Analysis of Imaging Profiles

As shown in Fig. 2, this paper presents a novel multifractal methodology to characterize and model AM images for quality control in 3D printing processes. First, the concept of "fractal dimension" is introduced to describe the average behaviors of image profiles. Second, we characterize local variations of image data using the multifractal spectrum. Third, the Hotelling T^2 statistics are extracted from the multifractal spectrum for the identification and characterization of defects in AM images.

3.1 Fractal Dimension. Fractals are irregular geometric objects that cannot be sufficiently specified using topological dimensions. Fractal objects are self-similar, i.e., if one zooms in or out the fractal set, its geometric shape has a similar appearance. Hence, fractal dimension is introduced to describe such "infinitely complex" fractal objects (or shape). Fractal sets have theoretical dimensions that exceed their topological dimensions and can be noninteger values. Fractal dimension specifies the complexity of a fractal object by measuring the changes of coverings relative to the scaling factor. It also characterizes the space-filling capacity of a fractal object with respect to its scaling properties in the space. In practice, the relationship between scaling and covering is often difficult to be determined. Generally, the variation of the number of coverings, $N(\epsilon)$, with respect to the scaling factor ϵ , is expressed as

$$N(\epsilon) \propto \epsilon^{-D}$$
 (1)

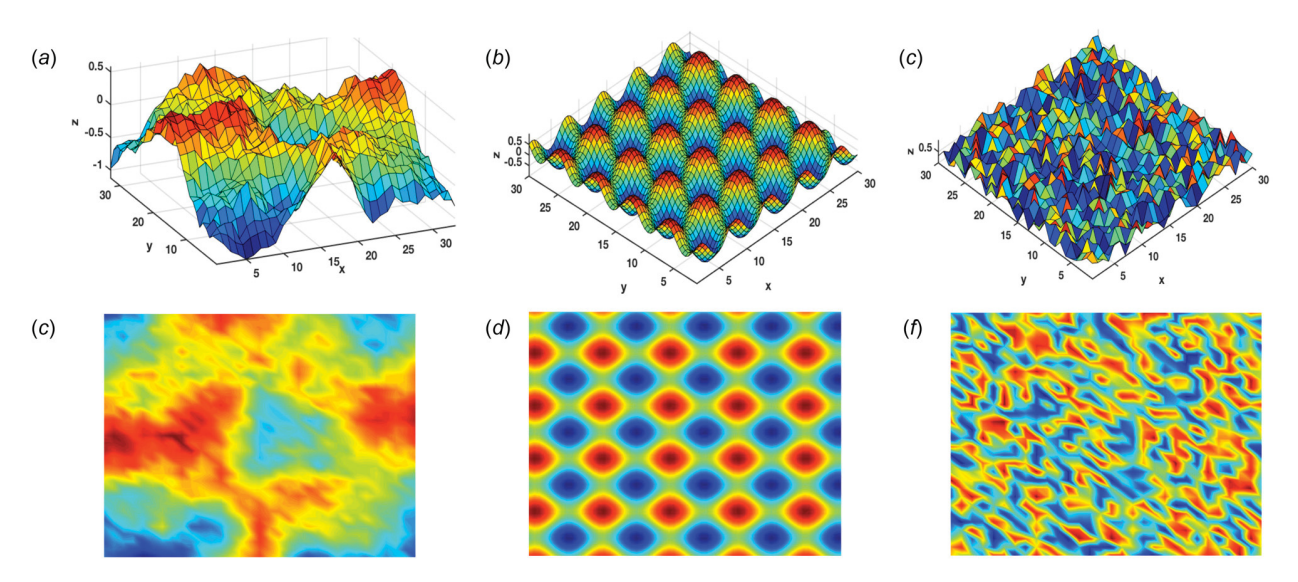


Fig. 1 Three different types of surfaces—(a) rough, (b) sinusoidal, (c) random, and their 2D images (d)—(f)

Journal of Manufacturing Science and Engineering

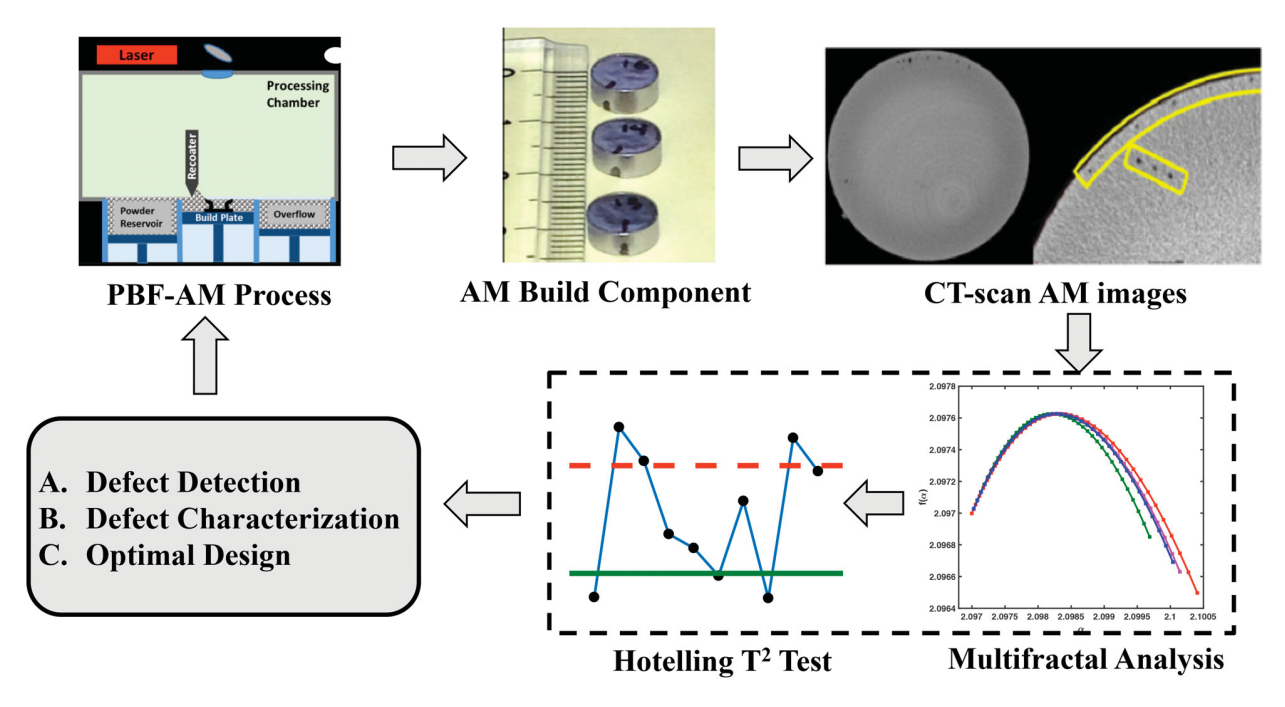


Fig. 2 Flowchart of research methodology

where D is the fractal dimension. Equation (1) is a scaling (or power) law that has been shown to describe the size distribution of many objects in nature. The so-called box-counting method is widely used to estimate the fractal dimension of an irregular object. The basic idea is to cover a fractal set with measure elements (e.g., box) at different sizes and examine how the number of boxes changes with respect to the size [33,34]. If N(a) is the number of boxes that are needed to cover a fractal object with the size a, then the box-counting dimension D_B is defined as

$$D_B := \lim_{a \to 0} \frac{\ln N(a)}{\ln (1/a)} \tag{2}$$

However, the monofractal analysis (i.e., a single fractal dimension) is limited in the ability to fully characterize complex scaling behaviors of many irregular objects in the real world [27]. The fractal dimension D characterizes the average behaviors of the image profiles via the scaling law, and profiles with different levels of roughness may have the same fractal dimension [35]. Therefore, monofractal analysis is limited in the ability to provide useful information on local fractal behaviors of the images.

3.2 Multifractal Spectrum. The multifractal analysis utilizes a spectrum of singularity exponents to provide a detailed and local description of complex scaling behaviors. In order to quantify local densities of the fractal set, we estimate the mass probability in the box centered at x_i of the image as

$$P_i(a) = N_i(a)/N \tag{3}$$

where $N_i(a)$ is the number of mass or pixels in the *i*th box of size a, N is the total mass of the set. It may be noted that the scaling of mass probability $P_i(a)$ with box size a of a multifractal set also follows the power law; it varies as:

$$P_i(a) \propto a^{\alpha_i}$$
 (4)

where α_i is the singularity exponent characterizing the local scaling in the *i*th box. In other words, these exponents represent local

fractal behaviors of the mass probability $P_i(a)$ around the center x_i of a box with size a, and it can be estimated from Eq. (4) as

$$\alpha_i = \alpha(x_i) = \lim_{a \to 0^+} \frac{\ln P_i(a)}{\ln a}$$
 (5)

The multifractal spectrum $f(\alpha)$ is the fractal dimension of the set of locations x's such that $\alpha(x) = \alpha$

$$f(\alpha) = D_F(\{x : \alpha(x) = \alpha\}) \tag{6}$$

where D_F is the fractal dimension. The multifractal spectrum $f(\alpha)$ provides a statistical distribution of singularity exponents α_i . Moreover, the number of boxes $N(\alpha)$ where the mass probability $P_i(a)$ has singular exponent value between α and $\alpha + \Delta \alpha$ also follows the power law with size a and multifractal spectrum $f(\alpha)$, i.e.,

$$N(\alpha) \propto a^{-f(\alpha)}$$
 (7)

Equation (7) is the generalized form of Eq. (1) for the multifractal sets. In addition, the multifractal spectrum is estimated from Eq. (7) as

$$f(\alpha) = \lim_{a \to 0} \frac{\ln N(\alpha)}{\ln (1/a)} \tag{8}$$

Traditionally, $f(\alpha)$ is estimated via the Legendre transformation [36] as

$$f(\alpha) = q\alpha - \tau(q)$$

$$\alpha(q) = d\tau(q)/dq$$
 (9)

where q is the moment and $\tau(q)$ is the mass exponent of the qth order moment. Moreover, the multifractal measures can be characterized by the scaling of the qth moments of $P_i(a)$ as

$$\sum_{i=1}^{N(a)} P_i^{q(a)} \propto a^{\tau(q)} = a^{(q-1)D_q}$$
 (10)

where $D_q = \tau(q)/(q-1)$ is the generalized fractal dimension. It may be noted that when q=0, Eq. (10) becomes $N(a) \propto a^{-D_0}$,

031014-4 / Vol. 140, MARCH 2018

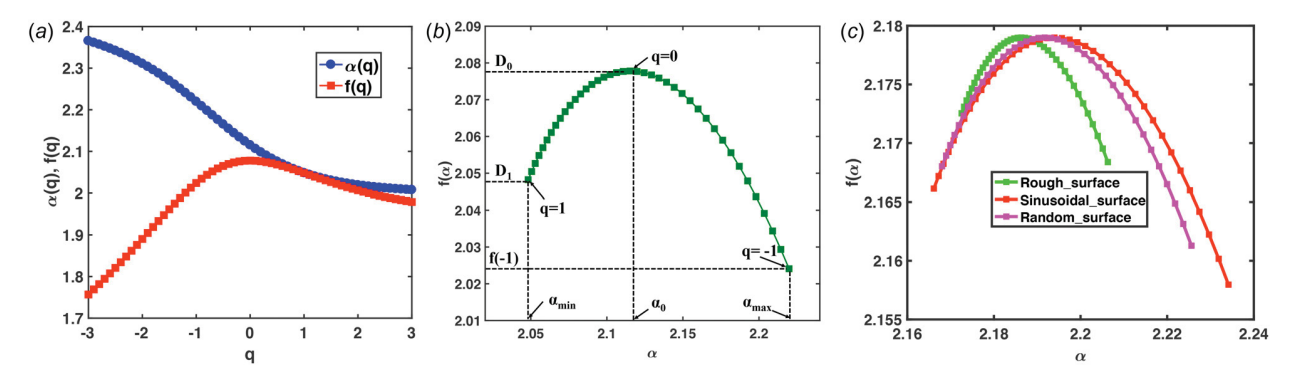


Fig. 3 (a) Illustration of f(q) and $\alpha(q)$ estimated in the range of q values from -3 to 3, (b) Illustration of $f(\alpha)$ spectrum, and (c) Multifractal spectra for the images of rough surface, sinusoidal surface, and random surface in Fig. 1

which is similar to Eq. (1). In other words, the generalized fractal dimension D_q is the same as box-counting dimension D_B when q=0. Moreover, when q=1 and q=2, the generalized fractal dimensions D_1 and D_2 are known as the entropy dimension and the correlation dimension, respectively. The entropy dimension characterizes the change of information entropy with the size of boxes, and the correlation dimension quantifies the correlation of measures in the boxes.

However, in order to determine the multifractal spectrum $f(\alpha)$ through Legendre transformation, one needs to first smooth the D_q curve and then use the Legendre transformation. The smoothing procedure not only causes additional errors to the estimation of $f(\alpha)$ but also misses phase transitions when it exhibits discontinuities. Therefore, we estimate the multifractal spectrum $f(\alpha)$ using a direct method [37]. A normalized measure $\mu_i(q, a)$ is defined as qth moments of mass probability $P_i(a)$

$$\mu_{i}(q, a) = \frac{P_{i}^{q}(a)}{\sum_{i=1}^{N(a)} P_{i}^{q}(a)}$$
(11)

Then, the multifractal spectrum $f(\alpha)$ can be directly computed as

$$f(\alpha(q)) = \lim_{a \to 0} \frac{\sum_{i=1}^{N(a)} \mu_i(q, a) \ln (\mu_i(q, a))}{\ln a}$$
 (12)

In addition, the average value of the singularity exponent $\alpha(q)$ can be computed with respect to $\mu_i(q,a)$ according to Eq. (5) as

$$\alpha(q) = \lim_{a \to 0} \frac{\sum_{i=1}^{N(a)} \mu_i(q, a) \ln \left(P_i^q(a)\right)}{\ln a}$$
(13)

Therefore, the multifractal spectrum $f(\alpha)$ and singularity exponent $\alpha(q)$ are implicit functions of the moments q. In other words, for each value of q, f(q) and $\alpha(q)$ are obtained from the slope of numerators of Eqs. (12) and (13) versus $\ln a$. Figure 3(a) shows the estimated $\alpha(q)$ and f(q) of the image shown in Fig. 1(d). Note that the two curves are tangent to each other at q=1, which is true according to Eqs. (11)–(13). Figure 3(b) shows the corresponding multifractal spectrum, where the maximum value of f(q) is found at q=0. Figure 3(c) shows the comparison of multifractal spectra of the images in Figs. 1(d)-1(f). It is worth noting that the spectrum is not symmetric with a long tail when q is negative. This is due to the fact that the variation of $f(\alpha(q))$ and $\alpha(q)$ with respect to q is more sensitive when q < 0 because of the probability $P_i(a)$ that is between 0 and 1.

3.3 Characterization of Multifractal Spectrum Using Hotelling T^2 **Statistics.** Furthermore, we propose to extract the Hotelling T^2 statistics from multifractal spectrum of image

profiles to determine whether there is a significant shift or change in the AM process. Let $F_{m \times p} = [f_1, f_2, ..., f_m]^{\mathrm{T}}$, and $A_{m \times p} = [\alpha_1, \alpha_2, ..., \alpha_m]^{\mathrm{T}}$, where $f_i = [f(q_1), f(q_2), ..., f(q_p)]^{\mathrm{T}}$, $\alpha_i = [\alpha(q_1), \alpha(q_2), ..., \alpha(q_p)]^{\mathrm{T}}$, m is the number of sample images, p is the length of q-vector, and $q_i \in [-1, 1]$. Then, the Hotelling T^2 statistics of f and α for sample i are defined as $T_f^2 = (f_i - \bar{f})^T \Sigma_f^{-1}(f_i - \bar{f})$ and $T_\alpha^2 = (\alpha_i - \bar{\alpha})^T \Sigma_\alpha^{-1}(\alpha_i - \bar{\alpha})$, respectively. Here, \bar{f} and $\bar{\alpha}$ denote the sample mean of f-feature and α -feature; Σ_f and Σ_α denote the sample covariance matrix of f-feature and α -feature, respectively. The upper control limit of Hotelling T^2 statistic is: UCL $= p(m+1)(m-1)/m^2 - mpF_{\alpha,p,m-p}$, where $F_{\alpha,p,m-p}$ is the upper $100\alpha\%$ of F distribution with degrees-of-freedom of p and m-p.

However, the dimensionality of feature vectors is large and thereby potentially leads to the issue of "curse of dimensionality." In order to reduce the dimensionality, the feature matrix F or A is projected into its eigenspace using the singular value decomposition, and a set of linearly independent principal components is used to represent the original feature space. Specifically, taking the F matrix as an example, F is first centered by subtracting the sample mean as $F_c = [f_1 - \bar{f}, f_2 - \bar{f}, ..., f_p - \bar{f}]^T$. Then, F_c is decomposed as $F_c = U\lambda V^T$, where U and V are $m \times m$ and $p \times p$ orthonormal matrices, respectively. λ is a matrix with nonzero elements in the diagonal, with $\lambda_{11} \ge \lambda_{22} \ge ... \ge \lambda_{pp} \ge 0$, which are the eigenvalues of F_c . The corresponding principal components are defined as $Z = F_c * V = U\lambda V^T V = U\lambda$. Moreover, the original feature matrix can be reconstructed as $F_c = ZV^{-1} = ZV^T$. Then, the sample covariance matrix can be reformulated as

$$\Sigma = \frac{F_c^{\mathsf{T}} F_c}{m-1} = \frac{V \mathbf{Z}^{\mathsf{T}} \mathbf{Z} V^{\mathsf{T}}}{m-1} = \frac{V \lambda^{\mathsf{T}} \lambda V^{\mathsf{T}}}{m-1} = \frac{\operatorname{diag}(\lambda^2)}{m-1}$$
(14)

where $\operatorname{diag}(\lambda^2)$ is a diagonal matrix whose elements are λ_{ii} , i = 1, 2, ..., p. Then, the T^2 statistic can be calculated as

$$T_i^2 = \mathbf{Z}_i \mathbf{V}^{\mathsf{T}} \mathbf{\Sigma}^{-1} \mathbf{V} \mathbf{Z}_i^{\mathsf{T}} = (m-1) \mathbf{Z}_i \mathbf{V}^{\mathsf{T}} \operatorname{diag}(\lambda^{-2}) \mathbf{V} \mathbf{Z}_i^{\mathsf{T}}$$
$$= (m-1) \sum_{k=1}^{p} \frac{\mathbf{Z}_{ik}^2}{\lambda_{kk}^2}$$
(15)

Accounting for the first s (s < p) principal components, the Hotelling T^2 statistic becomes

$$T_s^2(i) = (m-1) \sum_{k=1}^{q} \frac{\mathbf{Z}_{ik}^2}{\lambda_{bk}^2}$$
 (16)

The Hotelling statistics T^2 is then utilized to characterize the differences in multifractal spectra f(q) and $\alpha(q)$ of AM image profiles. The proposed approach of multifractal analysis will be evaluated and validated in experimental studies detailed in Sec. 4.

Journal of Manufacturing Science and Engineering

4 Materials and Experimental Design

In this investigation, we evaluate and validate the proposed methodology with both simulation study and real-world application. Materials and experimental details are described in Secs. 4.1 and 4.2.

- **4.1 Simulation Study.** In order to evaluate the monitoring performance of multifractal analysis for image profiles, three types of patterns are simulated, i.e., single-cluster, matern-cluster, and line patterns. For each type of pattern, we also simulated four levels of dispersion, i.e., L4, L3, L2, and L1. Note that, 100 realizations are generated for each dispersion level of each pattern. Examples of the generated patterns are shown in Fig. 4, and the detailed procedure is illustrated as follows:
 - (1) Single-cluster patterns: These patterns are divided into two parts. One is r% of points, following a Poisson distribution, generated within a circle at the center of the study region. And another is the remaining (100 r)% of points, also following a Poisson distribution, generated within the entire region. Four levels of r are considered in the simulation studies, i.e., 80(L4), 70(L3), 60(L2), and 50(L1), respectively.
 - (2) Matern-cluster patterns: These patterns are generated by two steps. First, ten parent points are generated with a Poisson distribution. Second, each parent point is replaced by ten random points within a circle of radius r_m. Four levels

- of radius r_m are considered as follows: 0.05(L4), 0.1(L3), 0.2(L2), and 0.3(L1), respectively.
- (3) Line patterns: These patterns also follow two steps: we first generate points following Poisson's distribution on two cross lines. Then, each point is randomly moved within a circle of radius r_l centered at its original location. Four levels of radius r_l are as follows: 0.02(L4), 0.05(L3), 0.1(L2), and 0.15(L1), respectively.

4.2 Real-World Application in Additive Manufacturing. In the present investigation, the proposed multifractal analysis is further implemented to analyze image data from a PBF-AM build fabricated at the CIMP-3D of the Pennsylvania State University. The AM build in Fig. 5(a) is fabricated in a direct metal laser sintering process that is carried out inside the EOS M280 system and parts are coated with an epoxy layer to prevent outgassing from the high-vacuum environment.

The CT scans of the studied AM build in Fig. 5(a) were collected with a GE vTomex M300 microfocus X-ray CT scanner, and are processed using the Volume Graphic software to extract the 2D image profiles of every layer in the 3D AM builds, as shown in Figs. 5(b) and 5(c). These images are 817×812 pixels with a pixel size of 176.25μ m. We studied three types of simulated defects, designated here as balling, crack, and pore, that were included as modifications to the AM image profiles in order to evaluate the performance of multifractal spectrum for the detection and characterization of AM defects. In addition, we

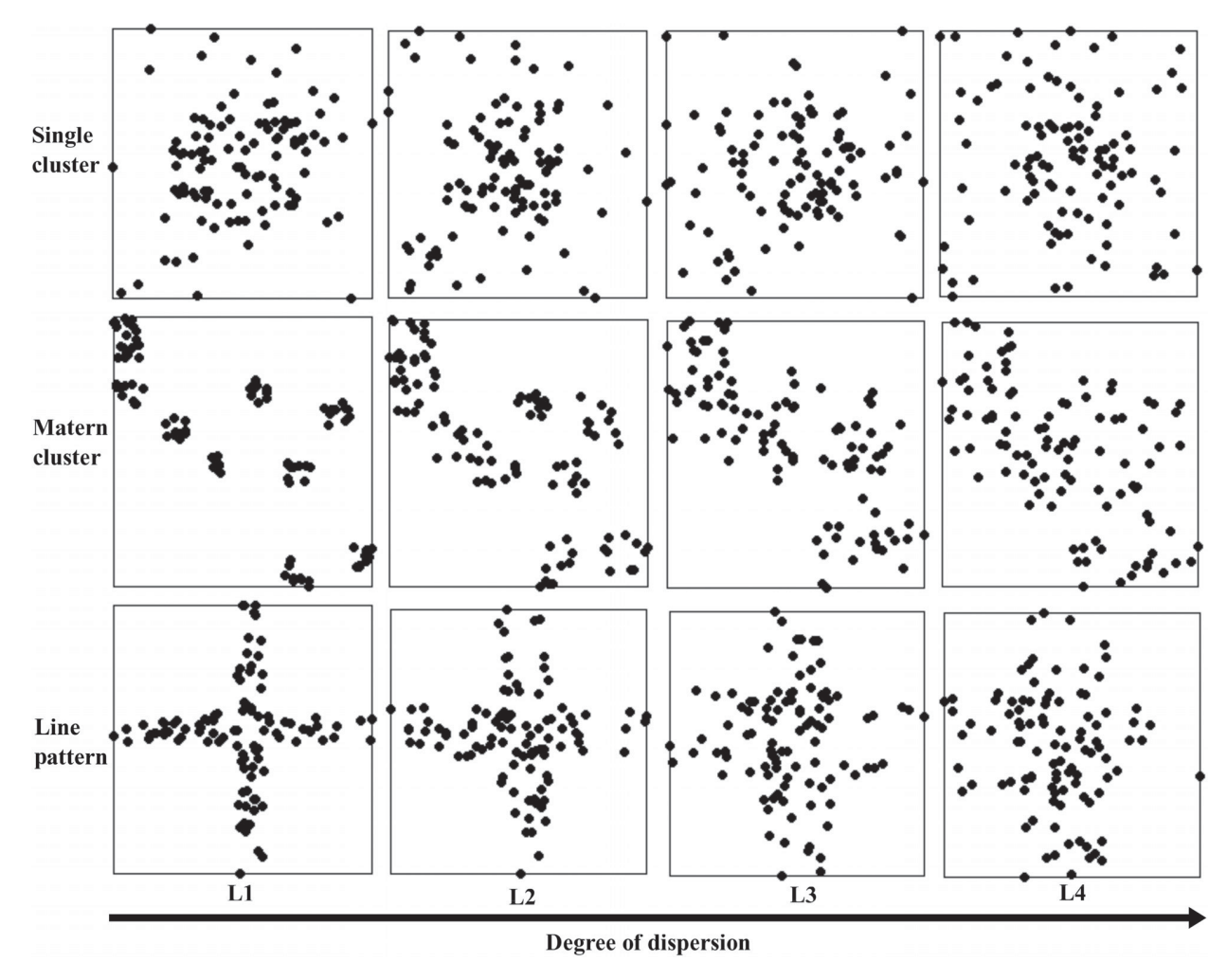


Fig. 4 Examples of simulated patterns with varying degrees of dispersion

031014-6 / Vol. 140, MARCH 2018

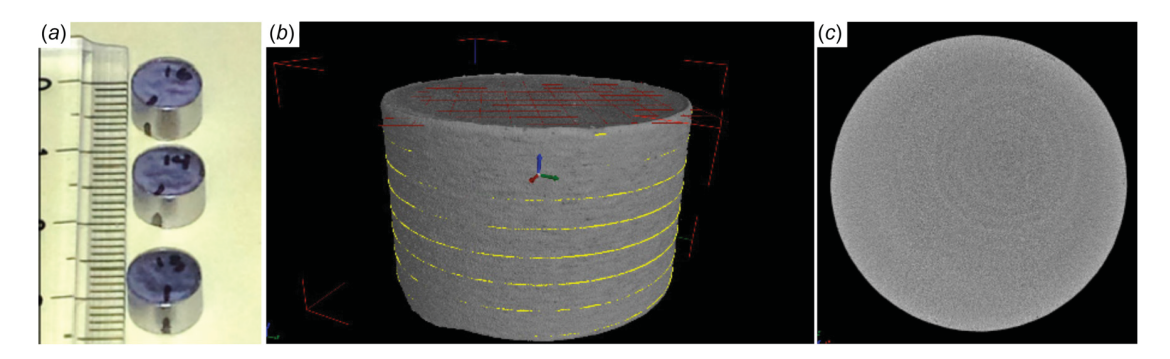


Fig. 5 (a) Actual build components from the AM process, (b) 3D visualization of CT scan, and (c) sliced CT-scan image

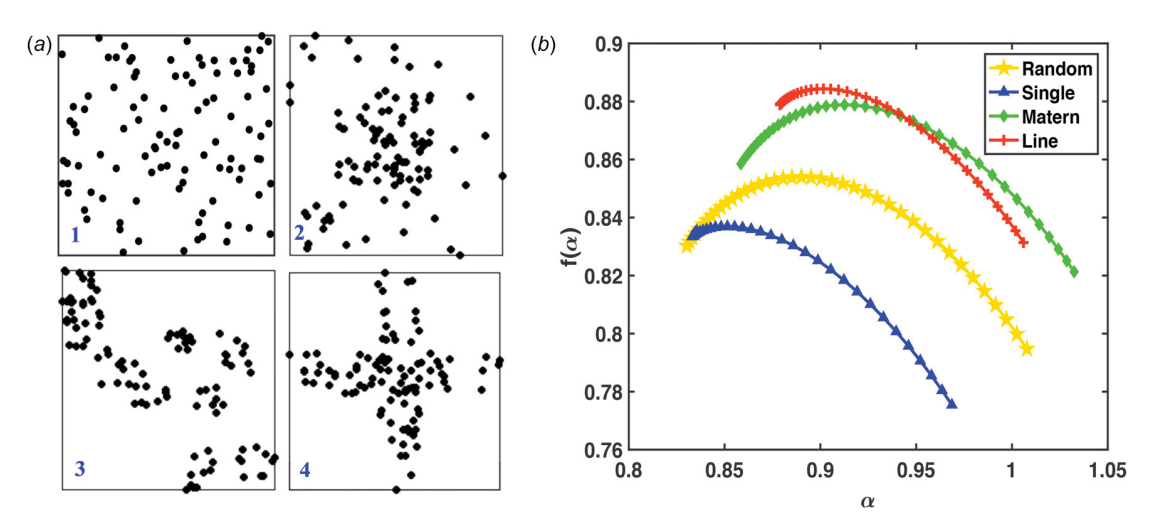


Fig. 6 (a) Four different types of simulated images: 1-random pattern, 2-single cluster, 3-matern cluster, and 4-line pattern (Note: the graphs of 2, 3, and 4 are with dispersion level of L2) and (b) multifractal spectra of the four different graphs

investigate the effect of PBF printing conditions, i.e., hatch spacing (H), scan velocity (V), and laser power (P), on the multifractal characteristics of defect patterns in AM image profiles using the multivariate regression analysis.

5 Experimental Results

5.1 Simulation Study. Three types of simulated patterns are studied in the present investigation, i.e., single-cluster patterns with one single cluster in the center, matern-cluster patterns with ten clusters, and line patterns with two-line-cross-shape clusters. Four levels of dispersion for each type of patterns are considered in the present investigation.

Figure 6(b) shows the multifractal spectra of the three simulated patterns, i.e., single-cluster, matern-cluster, and line patterns at dispersion level L2 as shown in Figs. 6(b)–6(d), together with the pattern that is completely random as shown in Fig. 6(a). Each spectrum is an average of 100 samples of each pattern. It may be noted that each pattern demonstrates different spectrum shape, which indicates that multifractal spectrum is able to differentiate the pattern of different images. Note that the single fractal dimensions D_0 , i.e., the maximum value of $f(\alpha)$ and the spectrum range are significantly different from each other in this simulation study.

Figure 7 illustrates the variation of D_0 with respect to dispersion levels for the three simulated patterns. Notably, the single fractal dimension D_0 decreases monotonically as the degrees of dispersion increase for all simulated patterns, i.e., single-cluster, matern-cluster, and line patterns. Such results agree very well

with the definition of D_0 in Eq. (2). According to Eq. (2), when the scale of the counting box a is small enough, the numbers of boxes covering the simulated images under different dispersions will be the same. When the scale a increases, the numbers of covering box will decrease for all the simulated images. However, the more dispersed images require more counting boxes to cover the entire area than the less dispersed images, which leads to a smaller slope of $\ln N(a)$ with $\ln (1/a)$, i.e., a smaller D_0 . It is worth noting

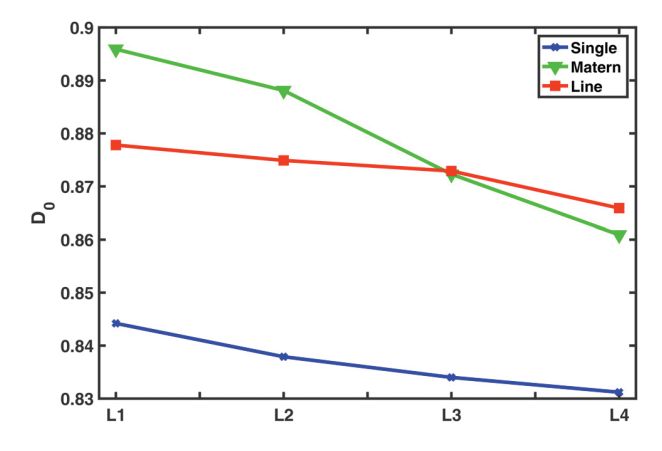


Fig. 7 The variation of single fractal dimension D_0 with respect to the dispersion level

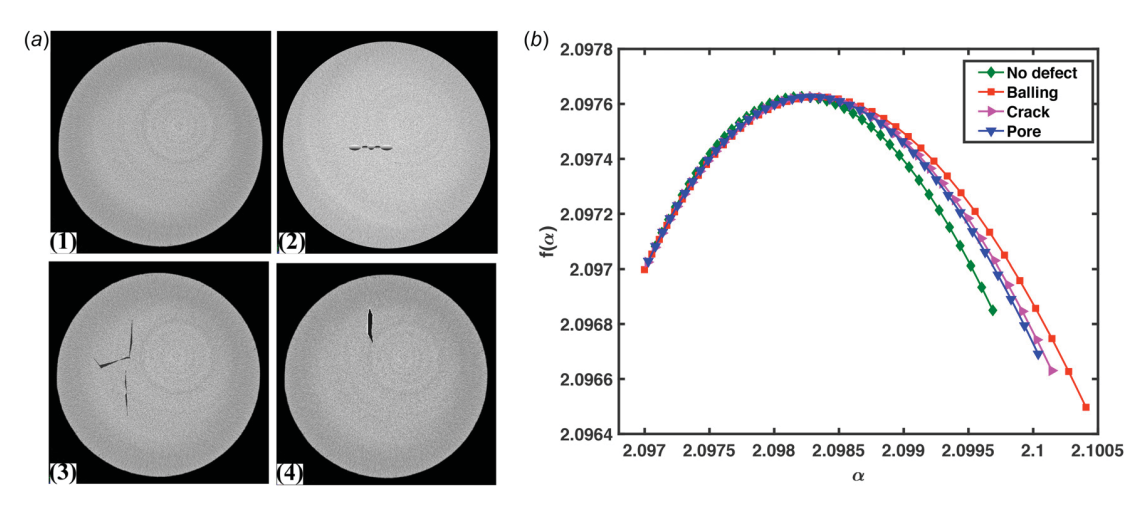


Fig. 8 (a) AM image profiles. (Note: 1 — with no defect; 2 — with balling defect; 3 — with crack defect; 4 — with pore defect.) and (b) multifractal spectrum of each image in (a).

Table 1 T^2 statistic and multifractal dimensions of AM images with no defect and with balling, crack, and pore defects

Туре	T_{α}^{2}	T_f^2	α(-1)	α(0)	α(1)	f(-1)	f(0)	$\alpha(-1) - \alpha(1)$	$D_1 - f(-1)$
No defect Balling Crack Pore	4.9 5.932E4 6.287E3 1.036E3	4.9 5.936E4 6.344E3 1.037E3	2.09969 2.10066 2.10014 2.10004	2.09821 2.09843 2.09829 2.09828	2.09708 2.09689 2.09702 2.09703	2.09685 2.09643 2.09663 2.09669	2.09763 2.09763 2.09763 2.09763	2.61×10^{-3} 3.77×10^{-3} 3.12×10^{-3} 3.01×10^{-3}	2.4×10^{-4} 4.6×10^{-4} 3.9×10^{-4} 3.4×10^{-4}

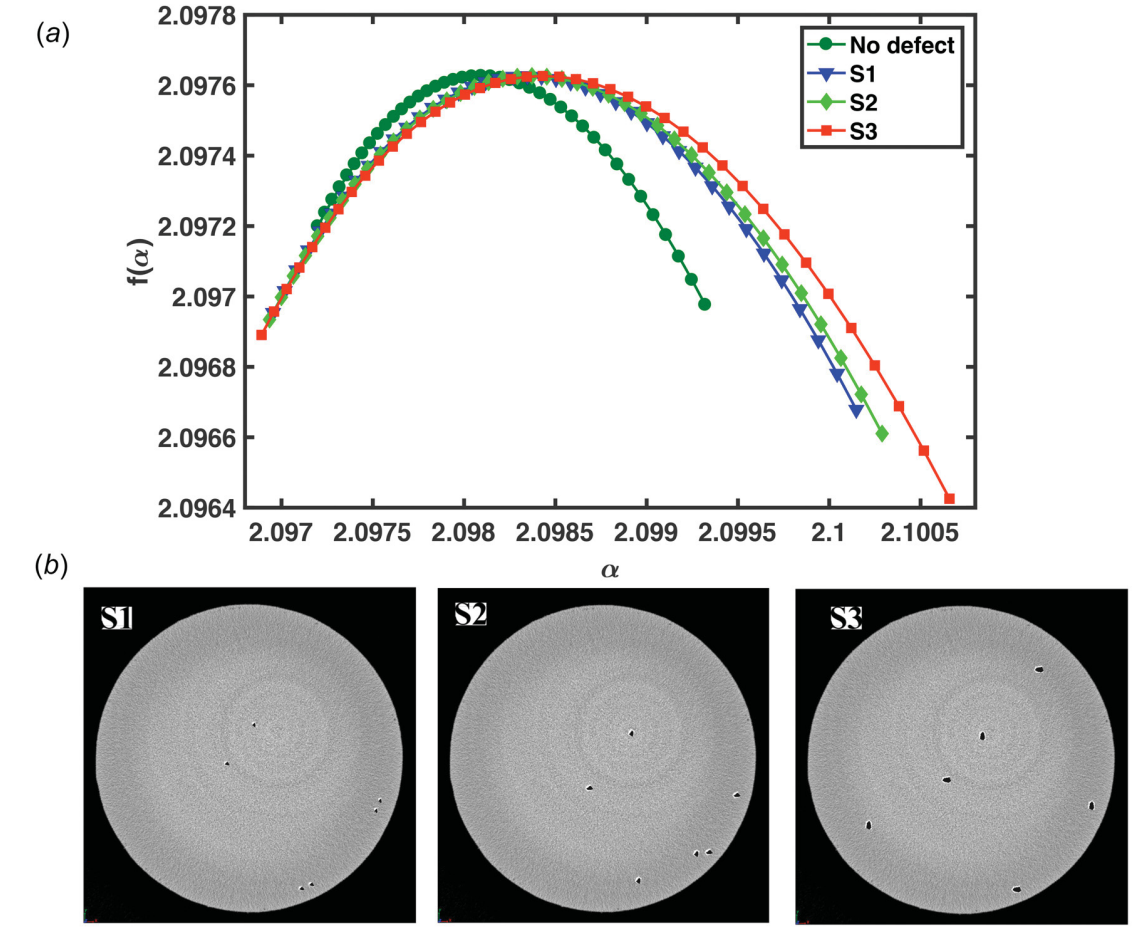


Fig. 9 Spectra of images with different sizes of pore defects

031014-8 / Vol. 140, MARCH 2018

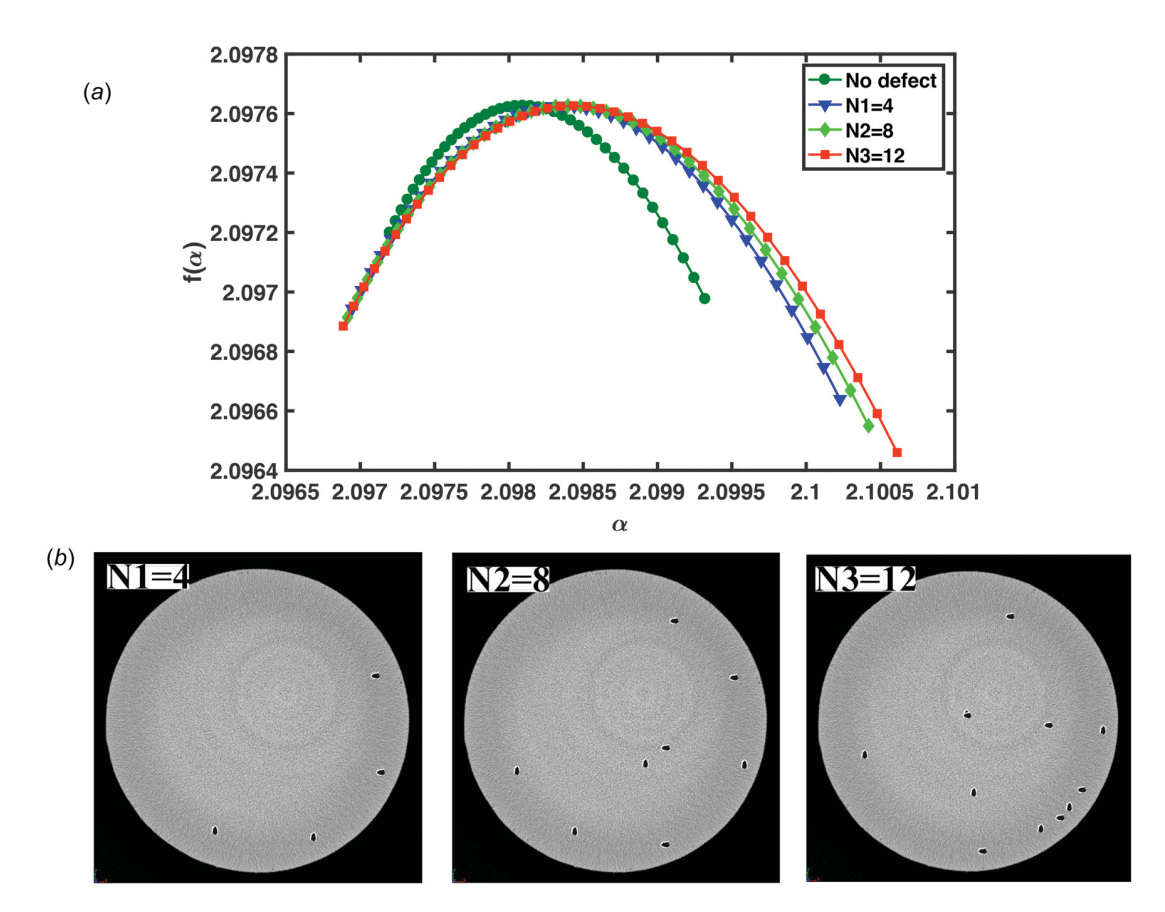


Fig. 10 Spectra of images with different number of pore defects

Table 2 T2 statistics and multifractal dimensions of AM images with pore defect of different size and different number

		T_{α}^{2}	T_f^2	α(-1)	α (0)	α(1)	f(-1)	f(0)	$\alpha(-1)$ - $\alpha(1)$	$D_1 - f(-1)$
Number	N1	1.593E3	1.586E3	2.10023	2.09836	2.09694	2.09664	2.09763	3.29×10^{-3}	3.0×10^{-4}
	N2	6.189E3	6.164E3	2.10042	2.09840	2.09691	2.09655	2.09763	3.51×10^{-3}	3.6×10^{-4}
	N3	1.368E4	1.364E4	2.10061	2.09843	2.09689	2.09646	2.09763	3.72E-3	4.3×10^{-4}
Size	S1	278	279	2.10015	2.09835	2.09695	2.09668	2.09763	3.20×10^{-3}	2.7×10^{-4}
	S2	2.80E3	2.79E3	2.10029	2.09837	2.09693	2.09661	2.09763	3.36×10^{-3}	3.2×10^{-4}
	S3	5.93E4	5.94E4	2.10066	2.09843	2.09689	2.09643	2.09763	3.77×10^{-3}	4.6×10^{-4}

that the single fractal dimension of matern-cluster and line pattern are greater compared to that of single-cluster, which is also due to the fact that single-cluster pattern is more dispersed than matern-cluster and line patterns. The experimental results show that the single fractal dimensions extracted from the simulated image data are significant indicators of the degree of dispersion and the multi-fractal spectrum has strong potentials to fully differentiate different patterns in AM images and can be further implemented to characterize the defect patterns in AM build component.

5.2 AM Applications—Defect Characterization and Detection

5.2.1 Multifractal Analysis of Different Types of Defects. As shown in Fig. 8(a), we studied three types of simulated defects designed to represent possible results from balling, cracking, or porosity that were added to individual images extracted from the post-build CT-scan of real parts. Note that 100 images of each type of defect and 100 images with no defects are analyzed. Figure 8(b) shows the corresponding multifractal spectra. Notably,

the multifractal analysis of the image with no defect shows a shorter right tail compared with the ones with defects, which is consistent with the fact that the AM CT-scan image with defects is more heterogeneous than the one with no defect. It is worth noting that the spectrum of the balling defect has the longest right tail, and the one with pore defect has a relatively shorter tail in the spectrum. It may be also noted that the value of D_0 (i.e., $f(\alpha_0)$) is around 2.09763 for all the cases. This is due to the fact that $D_0 = \lim_{\alpha \to 0} \ln N(\alpha) / \ln(1/\alpha)$ when q = 0, and all the post-build CT-scan images share the same image size. This suggests that the dimension of single fractal, i.e., D_0 , is not sufficient to characterize the defects in real-world CT-scan images.

The heterogeneity of the images can be assessed by the magnitude of differences in the values of D_1 and f(-1) or in the values of α_{-1} and α_1 . The difference $D_1 - f(-1)$ in the $f(\alpha)$ axis and $\alpha_{-1} - \alpha_1$ in the α axis indicate the heterogeneity of an image, which can be further used to differentiate the type and size of defects in image profiles. Table 1 shows the T^2 statistics of f-feature and α -feature and multifractal dimensions of four different kinds of images (i.e., with no defect, with balling, crack, and pore defects). The 5%

Journal of Manufacturing Science and Engineering

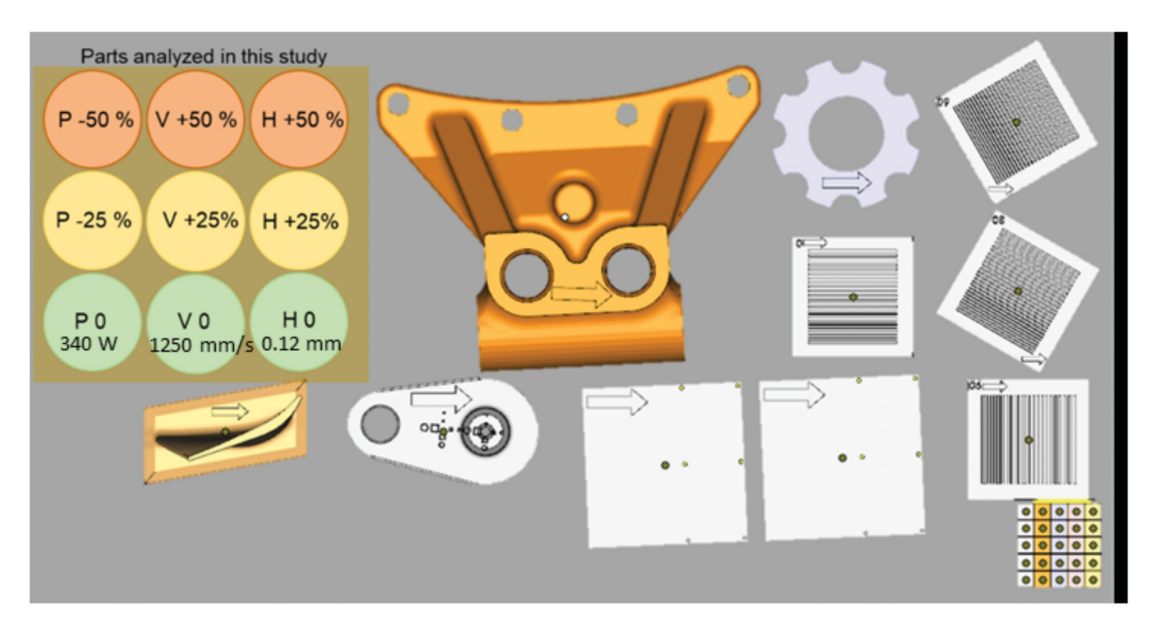


Fig. 11 Layout of the build setup. Note: The top left corner is the design of experiments to print seven groups of parts under different process conditions, i.e., (H_0, V_0, P_0) , $H25^+ = ((1+25\%)H_0, V_0, P_0)$, $H50^+ = ((1+50\%)H_0, V_0, P_0)$, $H50^+ = (H_0(1+50\%)H_0, V_0, P_0)$, and $H50^- = (H_0, V_0(1-50\%)H_0, P_0)$.

UCLs for both the α and f features are 12.16. Both T_f^2 and T_α^2 of the images with defects are significantly higher than the UCL, indicating a significant inhomogeneity level. In addition, $D_1 - f(-1)$ and $\alpha_{-1} - \alpha_1$ are the smallest for the image with no defect, and the post-build CT scan image with balling defects has the highest values of $D_1 - f(-1)$ and $\alpha_{-1} - \alpha_1$.

Furthermore, we conduct experiments to assess the effects of the size and number of defects on the shape of the multifractal spectrum. Figure 9(a) shows the multifractal spectra of images with no defect and with pore defect of three different sizes, i.e., S1, S2, and S3 as shown in Fig. 9(b). Figure 10(a) shows the multifractal spectra of images with no defect and with pore defect of three different numbers, i.e., N1 = 4, N1 = 8, and N1 = 12 as shown in Fig. 10(b). Notably, as the size of or the number of defects increases, the shape of the multifractal spectrum becomes more asymmetric. As shown in Table 2, when the size of defect increases from S1 to S3 or when the number of defects increases from N1 = 4 to N2 = 12, both $D_1 - f(-1)$ and $\alpha_{-1} - \alpha_1$ increase monotonically. In addition, the Hotelling T^2 statistics increase monotonically with the degree of defects in the image profiles. Such experimental results show that Hotelling T^2 statistic of the multifractal spectrum is an effective characteristic that captures the inhomogeneity of AM images. In Sec. 5.2.2, the Hoteling T^2 is further correlated with PBF-AM process parameters (i.e., hatch spacing, scan velocity, and laser power) to quantify the effects of different process conditions on the multifractal characteristics of AM images.

5.2.2 Impact of Process Conditions on Multifractal Characteristics of PBF-AM Images. Furthermore, we investigated the effect of PBF-AM process parameters on the multifractal characterization results of defect patterns in AM image profiles. The parts analyzed were printed by varying the hatch spacing (H), scan velocity (V), and laser power (P). Figure 11 outlines seven groups of parts under different process conditions. The nominal process condition is (H_0 , V_0 , P_0) = (0.12 mm, 1250 mm/s, 340 W). The other six process conditions are: $H25^+$ = ((1 + 25%) H_0 , V_0 , P_0), $H50^+$ = ((1 + 50%) H_0 , V_0 , P_0), $V25^+$ = (H_0 (1 + 25%), V_0 , P_0), $V50^+$ = (H_0 (1 + 50%), V_0 , P_0), $P25^-$ = (H_0 , V_0 (1 - 25%), P_0), and $P50^-$ = (H_0 , V_0 (1 - 50%), P_0).

In total, 120 CT-scan images are studied in the present investigation.

Figure 12 shows the multifractal spectra of 120 images under different printing conditions. It may be noted that the variations of printing conditions lead to distinct multifractal spectra. Each printing condition produces one group of multifractal spectra that are different from each other (e.g., color, range in Fig. 12). The 50% decrease in power (i.e., P50⁻) yields the most significant impact on multifractal characteristics (i.e., farthest from other groups in top right corner of Fig. 12). This implies that higher heterogeneity exists in the layers of AM parts under this printing condition. In addition, the increase in hatch spacing and velocity leads to the multifractal spectra that are different from the nominal condition (i.e., (H_0, V_0, P_0)). Such experimental results show that multifractal characteristics effectively reveal hidden features in PBF-AM images that are strongly correlated with the variations of printing conditions. This is conducive to the quality control of 3D AM processes.

Further, we develop a regression model to investigate the effects of process parameters on multifractal characteristics. In other words, we aim to study the relationship between (H, V, P) and Hotelling T^2 statistics using multivariate regression analysis. Here, the Hotelling T^2 statistic is calculated based on the combined features of f(q) and $\alpha(q)$. Before the regression analysis, we use the power transformation to transform the response variable y to improve variance stabilization and reduce the heteroscedasticity

$$z = f(y) = \begin{cases} \frac{y^{\lambda} - 1}{\lambda} & \lambda > 0\\ \log y & \lambda = 0 \end{cases}$$
 (17)

where y represents the Hotelling T^2 statistic. The optimal value λ^* is selected to be -0.0743181 that provides the most parsimonious model with no unusual patterns in the residual plots. Based on the transformed data z, the resulted model is as follows:

$$z = -66.80741 - 0.28893P + 0.09680V + 359.13189H + 0.00049P^2 + 0.00003V^2 - 853.08962H^2$$
 (18)

031014-10 / Vol. 140, MARCH 2018

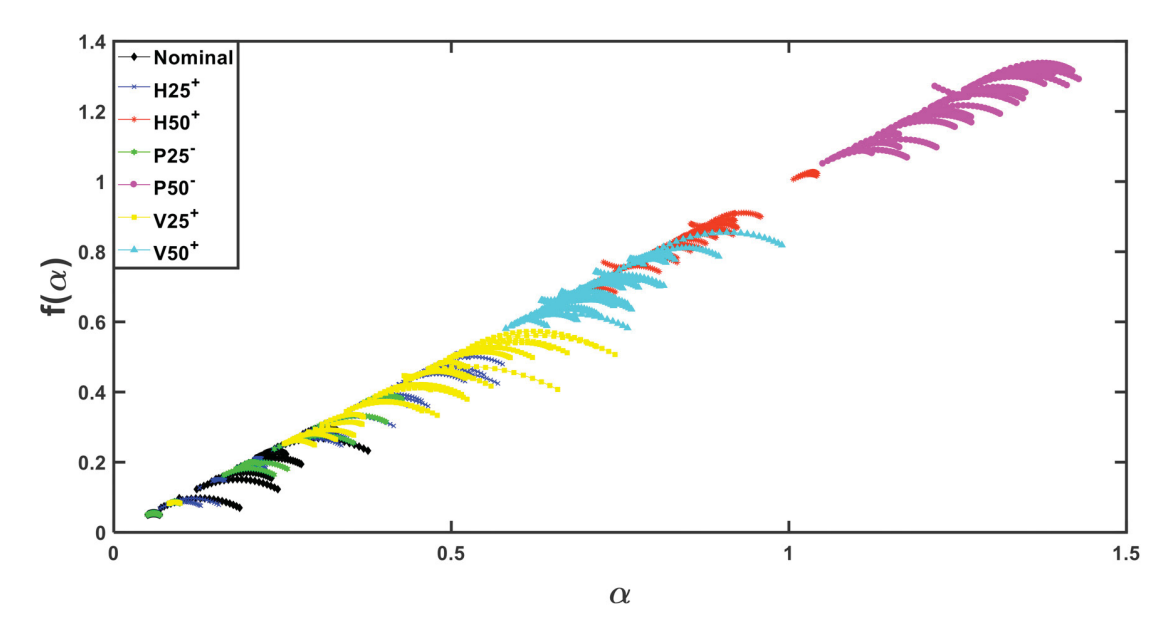


Fig. 12 Multifractal spectra of the 120 CT-scan images

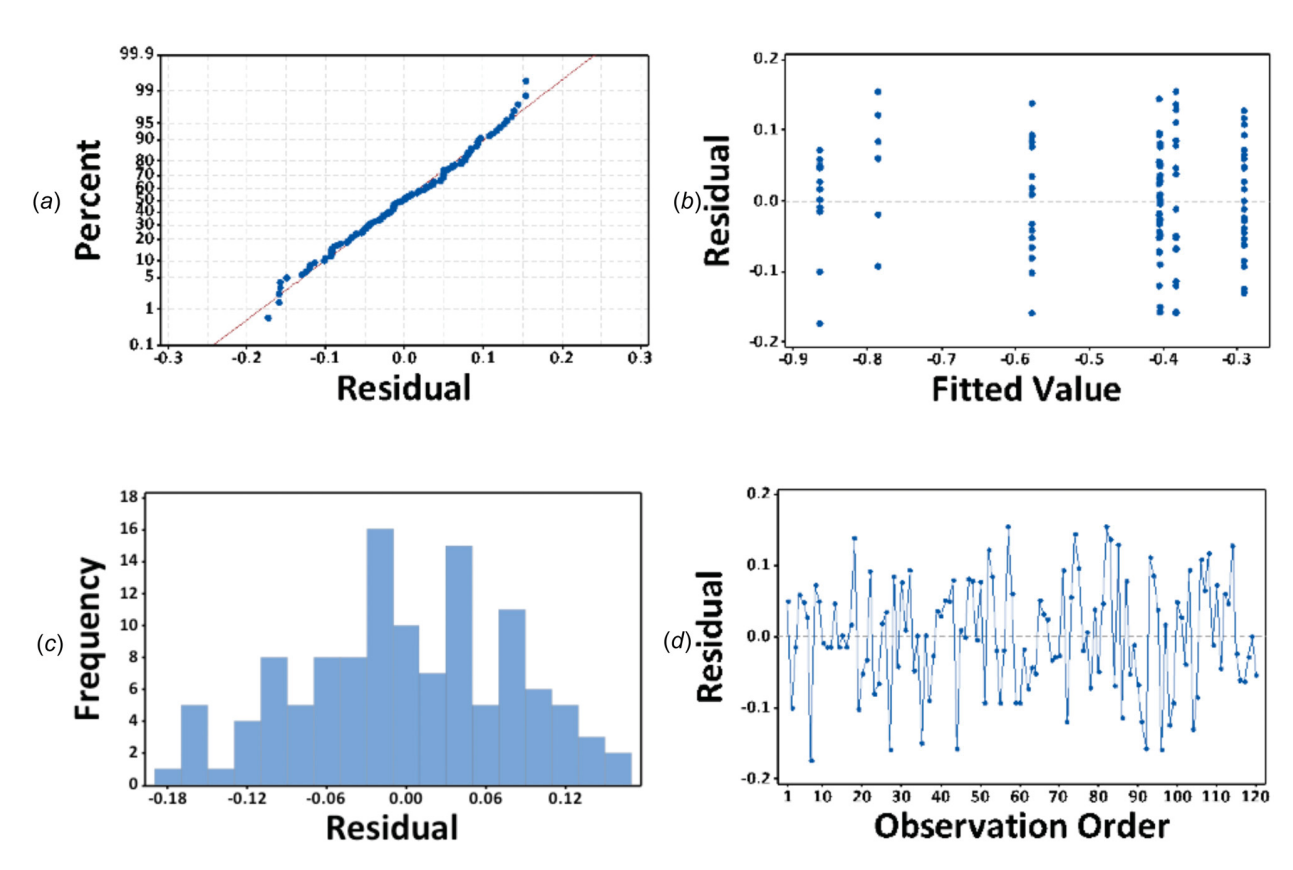


Fig. 13 Residual diagnosis of the regression model

Regression results show that this model is with $R^2 = 86.76\%$, and P, V, P^2 , and V^2 have p-value of zero, and H and H^2 have p-values of 0.002 and 0.024, respectively. All the parameters are significant in confidence level of 95%. It may also be noted that the power and velocity have more significant effects on the variation of Hotelling T^2 statistics than hatch spacing. Equation (18) shows that if we decrease the laser power, increase the scan velocity, and increase the hatch spacing from the nominal setting, Hotelling T^2

statistics will be increased. In other words, the heterogeneity of PBF-AM images is increased, which indicates an increasing level of defects. The regression results are consistent with the distribution of multifractal spectra in Fig. 12. Figure 13 shows the residual plots that provide diagnosis results of the regression model. There is no systematic pattern in the residual plots (i.e., Figs. 13(b) and 13(d)) and they show parallel bands centered around zero. In addition, the normal probability plot in Fig. 13(a) and the

Journal of Manufacturing Science and Engineering

histogram plot in Fig. 13(c) show that the normality assumption is validated.

6 Conclusions

Additive manufacturing techniques have been widely used to produce 3D parts with complex geometries. Quality control is one of the major bottlenecks in current AM practice. Realizing high levels of quality and repeatability calls for sensor-based monitoring and control of the AM process. Imaging sensing of 3D printing processes provides engineers with AM images containing rich information about both internal and external structures of AM builds. It is imperative to characterize and model image profiles for defect detection and quality control in AM processes. In traditional image-based methods, quality-related features, and characteristics are extracted after preprocessing the image profiles. The extracted features are further investigated for process monitoring and quality control. However, little has been done to investigate the nonlinear properties and fractal patterns inherent to the real-world image profiles for the monitoring and quality control in AM processes.

This paper proposes a novel approach of multifractal analysis of image profiles for quality control in AM processes. Multifractal analysis captures spatial variations inherent to AM images by resolving local densities and irregularities, and provides the characterization results in the form of multifractal spectrum. The Hotelling T^2 statistics of the multifractal spectrum represent the heterogeneity of image profiles (i.e., large values indicate higher heterogeneity), which can be further utilized to investigate the type and size of defects induced in AM parts. The performance of the proposed multifractal methodology is evaluated in both simulation study and real-world AM applications. In addition, we investigated the effect of PBF-AM process printing conditions (i.e., laser power, scan velocity, and hatch spacing) on the multifractal characterization results of defect patterns in AM image profiles. Experimental results show that the proposed multifractal approach effectively characterizes and detects the defects in layerwise AM image profiles. The laser power yields the most significant impact on multifractal characteristics than the scan velocity and hatch spacing. This work presents a new and effective approach to efficiently monitor AM processes and shows strong potential to help improve the levels of quality and repeatability of AM parts.

Acknowledgment

The views expressed in this paper are those of the authors and do not represent the official views of the NSF. The author (HY) also thanks Harold and Inge Marcus Career Professorship for additional financial support. We gratefully acknowledge the valuable contributions of the faculty, staff, and students at Penn State's CIMP-3D for providing the data utilized in this research.

Funding Data

 NSF Center for e-Design and NSF CAREER (Grant No. CMMI-1617148).

References

- Kruth, J.-P., Leu, M. C., and Nakagawa, T., 1998, "Progress in Additive Manufacturing and Rapid Prototyping," CIRP Ann.-Manuf. Technol., 47(2), pp. 525–540.
- [2] Tammas-Williams, S., Zhao, H., Léonard, F., Derguti, F., Todd, I., and Prangnell, P., 2015, "XCT Analysis of the Influence of Melt Strategies on Defect Population in Ti-6Al-4V Components Manufactured by Selective Electron Beam Melting," Materi. Charact., 102, pp. 47–61.
- [3] Li, R., Liu, J., Shi, Y., Wang, L., and Jiang, W., 2012, "Balling Behavior of Stainless Steel and Nickel Powder During Selective Laser Melting Process," Int. J. Adv. Manuf. Technol., 59(9–12), pp. 1025–1035.

- [4] Wang, F., Mao, H., Zhang, D., Zhao, X., and Shen, Y., 2008, "Online Study of Cracks During Laser Cladding Process Based on Acoustic Emission Technique and Finite Element Analysis," Appl. Surf. Sci., 255(5), pp. 3267–3275.
- [5] Rao, P. K., Liu, J. P., Roberson, D., Kong, Z. J., and Williams, C., 2015, "Online Real-Time Quality Monitoring in Additive Manufacturing Processes Using Heterogeneous Sensors," ASME J. Manuf. Sci. Eng., 137(6), p. 061007.
- [6] Chivel, Y., and Smurov, I., 2010, "On-Line Temperature Monitoring in Selective Laser Sintering/Melting," Phys. Procedia, 5(Pt. B), pp. 515–521.
- [7] Foster, B., Reutzel, E., Nassar, A., Hall, B., Brown, S., and Dickman, C., 2015, "Optical, Layerwise Monitoring of Powder Bed Fusion," Solid Freeform Fabrication Symposium, Austin, TX, Aug. 10–12, pp. 295–307.
- [8] Kleszczynski, S., Zur Jacobsmühlen, J., Sehrt, J., and Witt, G., 2012, "Error Detection in Laser Beam Melting Systems by High Resolution Imaging," 23rd Annual International Solid Freeform Fabrication Symposium, Austin, TX, Aug. 6–8, pp. 975–987.
- [9] Bi, G., Schürmann, B., Gasser, A., Wissenbach, K., and Poprawe, R., 2007, "Development and Qualification of a Novel Laser-Cladding Head With Integrated Sensors," Int. J. Mach. Tools Manuf., 47(3), pp. 555–561.
- [10] Reutzel, E. W., and Nassar, A. R., 2015, "A Survey of Sensing and Control Systems for Machine and Process Monitoring of Directed-Energy, Metal-Based Additive Manufacturing," Rapid Prototyping J., 21(2), pp. 159–167.
- [11] Krauss, H., Eschey, C., and Zaeh, M., 2012, "Thermography for Monitoring the Selective Laser Melting Process," 23rd Annual International Solid Freeform Fabrication Symposium, Austin, TX, Aug. 6–8, pp. 999–1014.
- [12] Rodriguez, E., Mireles, J., Terrazas, C. A., Espalin, D., Perez, M. A., and Wicker, R. B., 2015, "Approximation of Absolute Surface Temperature Measurements of Powder Bed Fusion Additive Manufacturing Technology Using in Situ Infrared Thermography," Addit. Manuf., 5, pp. 31–39.
- [13] Jacobsmühlen, J. Z., Kleszczynski, S., Schneider, D., and Witt, G., 2013, "High Resolution Imaging for Inspection of Laser Beam Melting Systems," IEEE International Instrumentation and Measurement Technology Conference (I2MTC), Minneapolis, MN, May 6–9, pp. 707–712.
 [14] Grasso, M., Laguzza, V., Semeraro, Q., and Colosimo, B. M., 2016, "In-
- [14] Grasso, M., Laguzza, V., Semeraro, Q., and Colosimo, B. M., 2016, "In-Process Monitoring of Selective Laser Melting: Spatial Detection of Defects Via Image Data Analysis," ASME J. Manuf. Sci. Eng., 139(5), p. 051001.
- [15] Pavan, M., Craeghs, T., Verhelst, R., Ducatteeuw, O., Kruth, J.-P., and Dewulf, W., 2016, "Ct-Based Quality Control of Laser Sintering of Polymers," Case Stud. Nondestr. Test. Eval., 6(Pt. B), pp. 62–68.
- [16] Dewulf, W., Pavan, M., Craeghs, T., and Kruth, J.-P., 2016, "Using X-Ray Computed Tomography to Improve the Porosity Level of Polyamide-12 Laser Sintered Parts," CIRP Ann.-Manuf. Technol., 65(1), pp. 205–208.
- [17] Megahed, F. M., Woodall, W. H., and Camelio, J. A., 2011, "A Review and Perspective on Control Charting With Image Data," J. Qual. Technol., 43(2), p. 83.
- [18] Nembhard, H. B., and Kao, M. S., 2001, "A Forecast-Based Monitoring Methodology for Process Transitions," Qual. Reliab. Eng. Int., 17(4), pp. 307–321.
- [19] Liang, Y.-T., and Chiou, Y.-C., 2008, "Vision-Based Automatic Tool Wear Monitoring System," Seventh World Congress on Intelligent Control and Automation (WCICA), Chongqing, China, June 25–27, pp. 6031–6035.
- [20] Graham, K., Krishnapisharody, K., Irons, G., and MacGregor, J., 2007, "Ladle Eye Area Measurement Using Multivariate Image Analysis," Can. Metall. Q., 46(4), pp. 397–405.
- [21] Jiang, B., Wang, C.-C., and Liu, H.-C., 2005, "Liquid Crystal Display Surface Uniformity Defect Inspection Using Analysis of Variance and Exponentially Weighted Moving Average Techniques," Int. J. Prod. Res., 43(1), pp. 67–80.
- [22] Kam, K. M., Zeng, L., Zhou, Q., Tran, R., and Yang, J., 2013, "On Assessing Spatial Uniformity of Particle Distributions in Quality Control of Manufacturing Processes," J. Manuf. Syst., 32(1), pp. 154–166.
- [23] Yan, H., Paynabar, K., and Shi, J., 2015, "Image-Based Process Monitoring Using Low-Rank Tensor Decomposition," IEEE Trans. Autom. Sci. Eng., 12(1), pp. 216–227.
- [24] Kan, C., and Yang, H., 2017, "Dynamic Network Monitoring and Control of in Situ Image Profiles From Ultraprecision Machining and Biomanufacturing Processes" Onal Reliab Eng. Int. epub.
- Processes," Qual. Reliab. Eng. Int., epub.

 [25] Kan, C., and Yang, H., 2015, "Network Models for Monitoring High-Dimensional Image Profiles," IEEE International Conference on Automation Science and Engineering (CASE), Gothenburg, Sweden, Aug. 24–28, pp. 1078–1083.
- [26] Jiang, X., Scott, P. J., Whitehouse, D. J., and Blunt, L., 2007, "Paradigm Shifts in Surface Metrology—Part II: The Current Shift," Proc. R. Soc. London, Ser. A, 463(2085), pp. 2071–2099.
- [27] Posadas, A. N., Giménez, D., Quiroz, R., and Protz, R., 2003, "Multifractal Characterization of Soil Pore Systems," Soil Sci. Soc. Am. J., 67(5), pp. 1361–1369.
- [28] Yang, H., Chen, Y., and Leonelli, F. M., 2016, "Characterization and Monitoring of Nonlinear Dynamics and Chaos in Complex Physiological Systems," *Healthcare Analytics: From Data to Knowledge to Healthcare Improvement*, H. Yang and E. K. Lee, eds., Wiley, Hoboken, NJ, pp. 59–93.
- [29] Chen, Y., and Yang, H., 2016, "Numerical Simulation and Pattern Characterization of Nonlinear Spatiotemporal Dynamics on Fractal Surfaces for the Whole-Heart Modeling Applications," Eur. Phys. J. B, 89(8), p. 181.
- [30] Kan, C., Cheng, C., and Yang, H., 2016, "Heterogeneous Recurrence Monitoring of Dynamic Transients in Ultraprecision Machining Processes," J. Manuf. Syst., 41, pp. 178–187.

- [31] Chen, Y., and Yang, H., 2016, "Heterogeneous Recurrence Representation and Quantification of Dynamic Transitions in Continuous Nonlinear Processes,"
- Eur. Phys. J. B, **89**(6), pp. 1–11.

 [32] Whitehouse, D. J., 2002, "Surface and Nanometrology, Markov and Fractal Scale of Size Properties," Seventh International Symposium on Laser Metrology Applied to Science, Industry, and Everyday Life, Novosibirsk, Russia, Sept. 9–13, pp. 691–707.
- [33] Foroutan-Pour, K., Dutilleul, P., and Smith, D. L., 1999, "Advances in the Implementation of the Box-Counting Method of Fractal Dimension Estimation," Appl. Math. Comput., 105(2–3), pp. 195–210.
- [34] Li, J., Du, Q., and Sun, C., 2009, "An Improved Box-Counting Method for Image Fractal Dimension Estimation," Pattern Recognit., 42(11), pp. 2460–2469.
 [35] Thomas, T., and Rosén, B.-G., 2008, "Implementation of Whitehouse's Method
- for Calculating Properties of Self-Affine Fractal Profiles," Proc. Inst. Mech. Eng., Part C, 222(8), pp. 1547–1550.
- Eng., Fart C., 222(8), pp. 154/–1550.
 [36] Halsey, T. C., Jensen, M. H., Kadanoff, L. P., Procaccia, I., and Shraiman, B. I., 1986, "Fractal Measures and Their Singularities: The Characterization of Strange Sets," Phys. Rev. A, 33(2), p. 1141.
 [37] Chhabra, A., and Jensen, R. V., 1989, "Direct Determination of the f (α) Singularity Spectrum," Phys. Rev. Lett., 62(12), p. 1327.